International Journal of Nanomedicine

Dovepress
Taylor & Francis Group

Open Access Full Text Article

ORIGINAL RESEARCH

Re-Mineralization By Polyelectrolyte Nanocomposite For Effective Against Dentin Hypersensitivity

Wenqi Gao[1,2], Chunyan Wan[1,2], Zeyu Han[2,3], Caiyun Li[1,2], Yanan Zhao[1,2], Lingshuang Liu[1,2]

[1]Department of Stomatology, The Affiliated Hospital of Qingdao University, Qingdao, 266003, People's Republic of China; [2]School of Stomatology, Qingdao University, Qingdao, 266023, People's Republic of China; [3]Department of Oral Implantology, The Affiliated Hospital of Qingdao University, Qingdao, 266003, People's Republic of China

Correspondence: Lingshuang Liu, Department of Stomatology, The Affiliated Hospital of Qingdao University, Qingdao, 266003, People's Republic of China, Email lais_1314@126.com

Introduction: Dentin hypersensitivity (DH) causes considerable discomfort in many patients due to its characteristic symptoms, which primarily arise from exposed dentinal tubules (DTs). DTs also serve as a pathway for bacterial invasion. Therefore, a treatment that both effectively occludes DTs and prevents caries is needed.

Methods: Polyaspartic acid (Pasp) and carboxymethyl chitosan (CMC) were combined with amorphous calcium phosphate (ACP) to develop PCA. PCA was compared with three polyelectrolyte complexes (PA, CA, PC). Recombinant collagen models assessed the mineralization-promoting effect of PCA, whereas DH models evaluated its ability to occlude DTs. The sealing performance and surface hardness of PCA-treated dentin discs were assessed by airtightness and hardness tests. Antibacterial effects were analyzed using live-dead staining, bacterial adherence assays, and colony-forming unit (CFU) counts. Biocompatibility was evaluated by live-dead cell staining, CCK-8 assays, and hemolysis tests.

Results: PCA contains ACP clusters approximately 2 nm in diameter and achieves effective intrafibrillar mineralization within 5 days. PCA completely covers the collagen fibers on the dentin surface and occludes the DTs. The remineralized dentin demonstrates excellent resistance to friction and acid exposure. PCA treatment significantly restores the airtightness and mechanical strength of demineralized dentin. Moreover, PCA exhibits strong antibacterial activity against Streptococcus mutans (*S. mutans*). Biocompatibility tests confirm favorable safety profiles.

Conclusion: This study demonstrates the dual function of PCA in DH management and caries prevention by occluding DTs and providing antibacterial protection, supporting its potential for clinical application.

Keywords: intrafibrillar mineralization, dentinal tubule, polyaspartic acid, carboxymethyl chitosan, amorphous calcium phosphate, antibacterial

Introduction

Dentin hypersensitivity (DH) is a prevalent and widely concerning problem in dentistry. This condition causes significant discomfort for patients and can severely affect quality of life, with a reported prevalence rate as high as 57% among adults.[1] DH arises due to exposed dentinal tubules (DTs), and various external factors may exacerbate the symptoms, such as daily exposure to temperature changes, chemical agents in the oral environment, and mechanical forces from chewing and toothbrushing.[2] Current clinical treatments primarily include pharmacological therapy, laser therapy, restorative approaches, and surgical interventions such as root canal treatment (RCT) for refractory cases.[3,4] However, these methods often demonstrate insufficient efficacy, limited duration of effect, or narrow applicability, which highlights the need for more effective treatment strategies in dental research.

Approaches to occlude DTs for the management of DH generally include surface ion precipitation to form a sealing layer, biomimetic remineralization to generate hydroxyapatite (HAP) crystals within the tubules, and protein precipitation for tubule

Received: 24 March 2025
Accepted: 7 August 2025
Published: 15 August 2025

Graphical Abstract

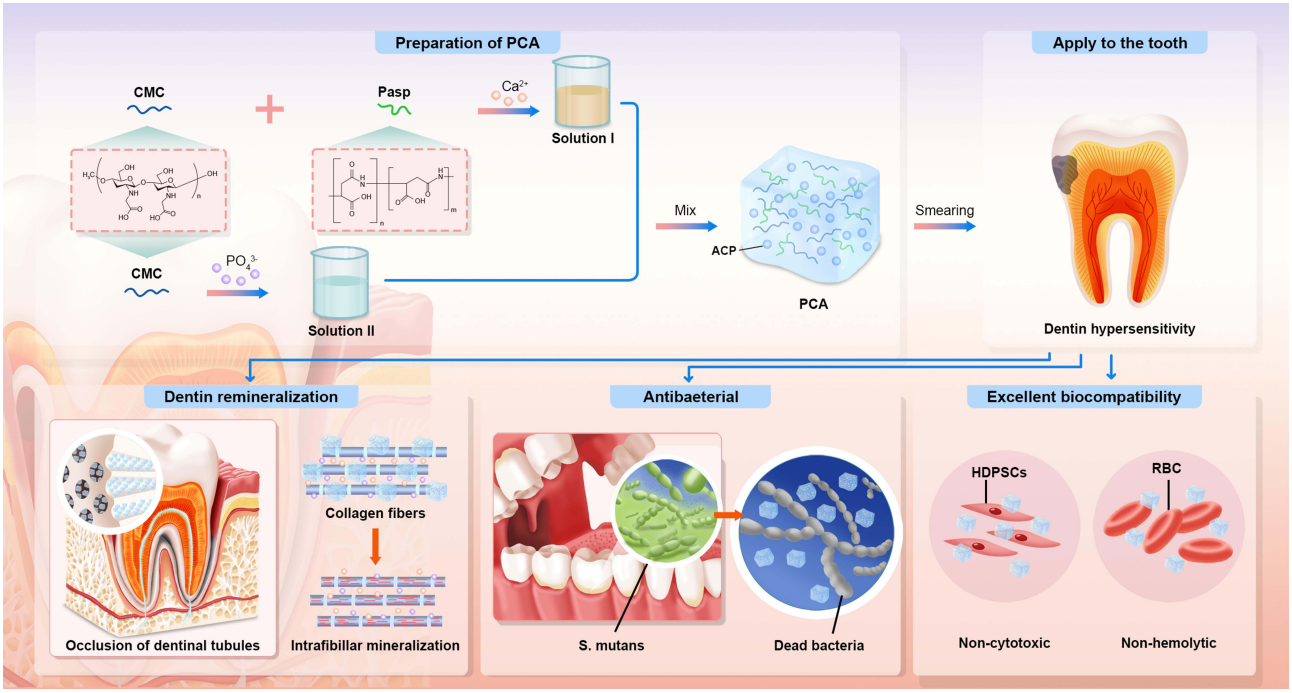

occlusion. Among these, biomimetic remineralization has attracted significant attention from researchers due to several advantages.[5,6] This approach closely mimics the natural physiological mineralization process,[7,8] and precise control over mineralization conditions allows the mineralized layer to exhibit excellent mechanical properties and stability, ensuring durable isolation from external stimuli, which is essential for alleviating DH symptoms.[9,10] Biomimetic approaches, such as microwave-synthesized chicken eggshell-derived nano-hydroxyapatite (CEnHAp) combined with phytosphingosine (PHS) or eggshell-derived nanohydroxyapatite (EnHA) combined with carboxymethyl chitosan (CMC), enable superior remineralization.[11,12] These strategies replicate natural mineralization processes, forming stable, high-performance mineralized layers that effectively block external stimuli, and offer promising therapeutic solutions for DH.

Dentin mineralization is classified into intrafibrillar and interfibrillar mineralization.[13] Intrafibrillar mineralization primarily refers to the deposition of minerals within the interstitial regions of collagen fibers and their orderly arrangement parallel to the c-axis of the fibers. In contrast, interfibrillar mineralization is characterized by the disordered deposition of minerals between collagen fibers.[14] Intrafibrillar mineralization is fundamental to dentin biomineralization and is generally more favorable.[15,16] Dentin sialophosphoprotein (DSPP), a critical non-collagenous protein (NCP), orchestrates dentin mineralization through its highly anionic domains. DSPP contains two functional domains: dentin sialoprotein (DSP) and dentin phosphoprotein (DPP). The phosphate and carboxyl groups in DPP specifically facilitate calcium binding and nucleation, whereas the protein's collagen-binding capacity directs intrafibrillar mineral deposition.[17,18] In addition to DSPP, amorphous calcium phosphate (ACP), collagen fibers, and other NCPs are essential during intrafibrillar mineralization.[19,20]

Polyelectrolytes, as NCP analogs, share similar structural and physicochemical properties,[21,22] enabling stabilization of nanoscale calcium phosphate in an amorphous phase and facilitating biomimetic mineralization.[23,24] For instance, the anionic polyaspartic acid (Pasp) mimics DSPP by trapping calcium ions (Ca^{2+}) via its amino ($-NH_2$) groups, forming stable ACP and promoting intrafibrillar mineralization.[25–27] Recent studies highlight the critical role of nanoscale calcium phosphate in enhancing intrafibrillar mineralization. Calcium phosphate particles stabilized by polyacrylic acid (PAA) and Pasp have achieved 95% collagen mineralization in vitro and demonstrated substantial regenerative effects in osteoporotic bone defects.[28]

Dentin, in contrast to enamel, contains a lower mineral content and is more vulnerable to cariogenic bacteria.[29] These bacteria and their metabolic byproducts can rapidly penetrate dentin and reach the root canals through exposed DTs, leading to infectious diseases in dentin, periodontium, pulp, and periapical regions.[30,31] The adhesion of cariogenic bacteria on the dentin surface also initiates continuous mineral dissolution and loss.[32,33] Most treatment strategies for DH focus on pain control, and insufficient attention is often paid to the bacterial challenges in exposed dentin. Effective bacterial control in the exposed dentin area should not be overlooked for patients with DH.

CMC is an amphoteric polyelectrolyte containing carboxyl (-COOH) and amino ($-NH_2$) functional groups, functioning as either an anionic or cationic polyelectrolyte depending on whether the pH is below or above its isoelectric point (PI = 3.5).[34,35] CMC has been shown to stabilize ACP at pH 7 and significantly promote the intrafibrillar mineralization of collagen fibers.[14,36] In addition, CMC possesses antimicrobial activity. It can inhibit the growth of various bacteria, such as Staphylococcus aureus (*S. aureus*) and Pseudomonas aeruginosa (*P. aeruginosa*), potentially by disrupting bacterial cell walls and membranes or inhibiting metabolic processes.[37] CMC can also form a uniform and stable film, providing favorable mechanical and barrier properties.[38]

In summary, this study aims to utilize Pasp and CMC to compete for Ca^{2+}, effectively inhibiting the rapid precipitation of Ca^{2+} and phosphate ions (PO_4^{3-}) and thereby forming highly stable nano-ACP. This mechanism not only synergistically regulates the directional growth and morphology of mineral crystals but also suppresses the proliferation of cariogenic bacteria through the antibacterial properties of CMC. By integrating the dual effects of DT occlusion and antibacterial action, this multifunctional composite is expected to achieve superior tubule sealing and antibacterial efficacy compared to traditional desensitizing agents. This strategy offers a new approach for the synergistic prevention and treatment of DH and dental caries.

Materials and Methods

Pasp (Rhawn, China), CMC (degree of substitution 0.8, degree of deacetylation 85%, molecular weight 100 kDa, Aladdin, USA), calcium chloride solution ($CaCl_2$, 2.5 mol/L, Macklin, China), dibasic sodium phosphate solution (Na_2HPO_4, 1.5 mol/L, Leagene, China), ethanol (analytical reagent grade, Sinopharm Chemical Reagent Co., Ltd., China), Tris-buffered saline (TBS, Solarbio, China), type I collagen lyophilized powder (rat tail, MedChemExpress, USA), acetic acid (analytical reagent, Sinopharm Chemical Reagent Co., Ltd., China), sodium hydroxide (NaOH, Aladdin, China), HEPES buffer (Biorigin, China), N-(3-dimethylaminopropyl)-N′-ethylcarbodiimide hydrochloride (EDC, Macklin, China), thymol (analytical reagent, Rhawn, China), ethylenediaminetetraacetic acid (EDTA, Solarbio, China), Gluma desensitizer (Gluma, Germany), artificial saliva (Leagene, China), citric acid (Codow, China), Brain Heart Infusion broth (BHI, Hopebio, China), agar powder (Solarbio, China), bacterial viability assay kit with DMAO and propidium iodide (PI) (Beyotime, China), phosphate-buffered saline (PBS, Pricella, China), fetal bovine serum (FBS, Pricella, China), penicillin-streptomycin solution (Pricella, China), α-MEM medium (Pricella, China), Cell Counting Kit-8 (MedChemExpress, USA), and Calcein AM/PI Double Staining Kit (Elabscience, China) were used in all experiments.

Preparation of Polyelectrolyte Complexes

At room temperature, 0.4 g/mL Pasp and 0.15 g/mL CMC solutions were first prepared. Next, 1.6 mL of CMC solution was combined with 0.27 mL of Pasp solution, followed by the addition of 0.5 mL $CaCl_2$ solution, and stirred thoroughly to obtain Solution I. Separately, 1.6 mL of CMC solution was mixed with 0.5 mL Na_2HPO_4 solution and stirred to obtain Solution II. The PCA composite was formed by mixing Solutions I and II with constant stirring. Control complexes were synthesized using the same method: PA without CMC, CA without Pasp, and PC without both $CaCl_2$ and Na_2HPO_4. The pH of all solutions was adjusted to neutral using 0.1 M NaOH or HCl.

Characterization of Polyelectrolyte Complexes

PCA, PA, CA, and PC samples were frozen at –80°C for 24 h and lyophilized using a freeze dryer (Alpha 2–4LSC BASIC, Germany) for another 24 h. The freeze-dried samples were dispersed ultrasonically in ethanol (20 kHz, 2 min), dropped onto transmission electron microscopy (TEM) copper grids, and observed using high-resolution TEM (HRTEM, JEM 2100F, Japan) at 100 kV. The diameter distribution of calcium phosphate nanoclusters was analyzed with ImageJ software. Crystalline

phases were identified by selected-area electron diffraction (SAED, JEM 2100F, Japan; camera length 100 cm, exposure 2 s). Surface morphology was examined by scanning electron microscopy (SEM, Tescan Vega3, Czech Republic) at 7 kV and 8 mm working distance. Elemental composition and distribution were evaluated by energy-dispersive spectroscopy (EDS, Oxford Instruments X-Max 50, Czech Republic) at 15 kV, 10 mm working distance, and 60s acquisition. X-ray diffraction (XRD, Ultima IV, Japan) was conducted over a 2θ range of 10–70° at 10°/min. Zeta potential was measured using a Zetasizer Nano ZS (UK) at 25°C and 13° scattering angle. Fourier transform infrared spectroscopy (FTIR, Nicolet iS50, USA) was used to characterize functional groups through 32 scans (wavenumber range: 400–4000 cm^{-1}, resolution: 4 cm^{-1}).

In vitro Release of Calcium and Phosphorus

To minimize interference from artificial saliva, simulated body fluid (SBF), and PBS, 1 mL of PCA, PA, and CA were each immersed in 10 mL TBS. To simulate physiological body temperature, the mixtures were stirred at 37°C for 10 min, then incubated under static conditions in TBS for 24 h. After incubation, samples were centrifuged at 4000 rpm for 10 min, and 5 mL supernatant was collected from each sample. The supernatants were subjected to microwave-assisted digestion prior to analysis. Quantitative determination of released calcium (Ca) and phosphorus (P) was performed using inductively coupled plasma optical emission spectrometry (ICP-OES, Agilent 5800).

Intrafibrillar Mineralization of Reconstituted Collagen

Type I collagen (1 mg/mL) was prepared by dissolving collagen lyophilized powder in 0.1 M acetic acid at 4°C. Two hundred-mesh nickel TEM grids were immersed in the collagen solution, and pH was adjusted to neutral with 1 M NaOH. HEPES buffer (pH 7.4) was added to promote collagen self-assembly, followed by immersion in 0.3 M EDC solution for 4 h to induce crosslinking. Grids were rinsed with ultrapure water and air-dried. For remineralization, 1 mL of PCA, PA, CA, and PC was each added to 10 mL ultrapure water and shaken for 30 min to release ACP. The nickel grids were immersed in each remineralization solution and incubated at 37°C for 1, 3, or 5 days. After mineralization, the grids were washed, negatively stained with uranyl acetate, and analyzed using TEM (JEM-1400Flash, Japan) to assess collagen mineralization and by SAED to determine the crystallinity of CaP minerals.

Preparation of DH Models

A power analysis was performed using G*Power 3.1 with an effect size of 0.4 and a significance level of $\alpha = 0.05$. The analysis determined that a minimum sample size of 90 would be necessary to achieve 80% statistical power for detecting significant effects. To enhance statistical power and accommodate potential attrition, the final sample size was increased to 120.

The protocol was approved by the Medical Ethics Committee of the Affiliated Hospital of Qingdao University (QYFYWZLL29632). After obtaining informed consent, 120 caries-free, crack-free third molars freshly extracted for orthodontic or occlusal reasons were collected within 1 month. Teeth were preserved in thymol solution at 4°C after removing root surface soft tissue and tartar with a curette. Dentin discs (5 × 5×1 mm) were prepared from the third molar along the long axis using a low-speed precision cutting machine (DTQ-5, China), with the distal pulpal surface as the experimental surface. Discs were sequentially polished with 600, 800, 1200, 2000, and 3000 grit silicon carbide sandpaper and rinsed in ultrapure water to achieve a smooth surface. Each disc was treated with 0.5 M EDTA (pH 8) for 5 min and ultrasonically cleaned with ultrapure water for 10 min.

Grouping of Demineralized Dentin Discs

Dentin discs were prepared following standardized protocols and sequentially numbered. To ensure unbiased allocation, a computer-generated randomization process was conducted under independent supervision. An investigator who did not participate in subsequent procedures generated the randomization schedule using a random number table, ensuring equal probability of assignment for each disc. Therefore, all dentin discs were randomly assigned to groups of 20 samples each: A (blank), B (Gluma desensitizer), C (PCA), D (PA), E (CA), and F (PC).

For Group A, the surface of each dentin disc was brushed for 60s, left to air dry, and rinsed with pressure-free ultrapure water. Group B received Gluma desensitizer applied for 60s with a small brush; the surface was rinsed with pressure-free ultrapure water after the liquid film disappeared and the surface lost its shine. Groups C, D, E, and F were

treated using the same protocol with PCA, PA, CA, and PC. All groups received daily treatment for 28 days and were stored in fresh artificial saliva at 37°C after each application.

SEM Observation of DT Occlusion

At 28 days of treatment, dentin discs were randomly selected from each group. After rinsing with ultrapure water, samples were dehydrated through a graded ethanol series (30%, 50%, 70%, 80%, 90%, 95%, and 100%). Drying was performed in a forced convection oven (DHG-9000, China) at 60°C. Gold sputter-coating was applied prior to SEM analysis to assess DT occlusion, and EDS was used to determine the calcium and phosphorus contents. After 28 days, additional dentin discs from each group were selected. To avoid affecting the experimental surface, each disc was sectioned from the untreated side to a depth of approximately 0.2 mm and split by external force. After further rinsing, dehydration, drying, and gold coating, SEM was used to observe tubule occlusion in cross-section. The resulting bisected sections were allocated to either acid immersion or abrasion resistance testing. Acid resistance was evaluated by immersing samples in 6% citric acid solution (pH 1.5) for 1 min. Abrasion resistance was assessed by simulated toothbrushing with a soft-bristled brush under controlled force (2 min per session, twice daily for 7 days). Treated discs were then rinsed, dehydrated, dried, gold coated, and examined by SEM.

The Examination of Dentin Airtightness

A modified airtightness device was employed to evaluate the macroscopic effect of tubule occlusion. Each dentin disc was clamped between two rubber rings with a central opening and fixed in the chamber. A droplet of water was placed in a tube connected to the chamber. Air was injected using a syringe, and a manometer recorded the air pressure at which water movement occurred, defined as the critical pressure. Higher pressure indicated lower dentin permeability and more effective occlusion. Three samples per group were tested, with five measurements for each sample. The airtightness test was repeated after acid and abrasion testing.

The Examination of Dentin Composition Hardness

Native dentin, demineralized dentin, and dentin discs from Groups A–F were tested for hardness using the Vickers hardness test (Wilson Tukon1102, USA). A diamond indenter (apex angle 136°) applied a load of 0.5 kgf for 10s. The length of the two diagonals of each indentation was measured microscopically. Three samples per group were tested, with three measurement points for each sample. The Vickers hardness value (HV) was calculated using the mean diagonal length and a standard reference table.

Preparation of Dental Plaque Biofilm

Streptococcus mutans (*S. mutans*, ATCC25175 = NCTC10449) was obtained from the Shanghai Biology Collection Center (SHBCC) for biofilm formation. The suspension of *S. mutans* was cultured anaerobically in BHI medium at 37°C with 5% CO_2. The optimal dilution (10^7 CFU/mL) was established, and 1% sucrose was added to the inoculation medium. Dentin discs treated for 28 days in Groups A, C, D, E, and F were sterilized by UV irradiation (254 nm) for 72 h, placed in 24-well plates with 1 mL inoculation medium, and incubated anaerobically at 37°C for 36 h to form biofilm. Discs were rinsed three times with PBS to remove non-adherent bacteria, transferred to new 24-well plates, and labeled accordingly.

Anti-Bacterial Activity

To the corresponding groups (A, C, D, E, F), 100 μL of ultrapure water, PCA, CA, or PC was added to their respective media containing biofilm-inoculated dentin discs. Plates were incubated anaerobically for 24 h. Following incubation, discs were rinsed three times with PBS, and the biofilms were stained with a bacterial viability assay kit (DMAO & PI) according to manufacturer instructions. Confocal laser scanning microscopy (CLSM, Olympus FV1200, Japan) was used to visualize live and dead bacteria, and quantitative analysis was performed with ImageJ.

To further assess the antimicrobial effect, incubated discs were fixed in 2.5% glutaraldehyde, rinsed, and dehydrated through graded ethanol. After drying and gold sputter-coating, samples were imaged by SEM. Three representative images per group were analyzed to evaluate bacterial adhesion.

For quantitative bacterial counts, biofilm was dislodged from each disc by vortexing in 3 mL PBS for 5 min. For further assessment, 0.1 mL of PCA, CA, and PC was co-cultured with 1 mL *S. mutans* suspension at 37°C for 12 and 24 h. Each suspension and the control were serially diluted in PBS (10^{-1} to 10^{-6}), and 100 μL was plated on BHI agar. Plates were incubated anaerobically at 37°C for 48 h, and colonies were counted. Each assay was performed in triplicate.

Cultivation of Human Dental Pulp Stem Cells

This study was conducted in accordance with ethical approval requirements (QYFYWZLL29632). After obtaining informed consent, 30 caries-free, crack-free premolars were collected from healthy adults aged 18–25 years, extracted for orthodontic or impaction reasons. Under sterile conditions, dental pulp tissue was isolated, and human dental pulp stem cells (HDPSCs) were harvested using the tissue explant method. Primary cultures were maintained in α-MEM complete medium supplemented with 10% FBS. Third-passage cells were analyzed for surface markers (CD73, CD90, CD105, CD34, CD45) by flow cytometry (CytoFLEX, China) to confirm compliance with international standards for dental pulp stem cell identification.

Cytotoxicity Test

Extracts of PCA, PA, CA, and PC were prepared at a 1:10 (v/v) ratio in culture medium. The mixtures were incubated at 37°C, 100 rpm for 72 h to facilitate extraction of leachable components. After incubation, the extracts were filtered through a 0.22 μm sterile membrane to remove particulates, yielding final extracts for further use.

Third-passage HDPSCs (1×10^5 cells) were resuspended in 2.5 mL medium and seeded into 35 mm glass-bottom dishes. After 24 h of incubation at 37°C in a humidified 5% CO_2 environment, the medium was replaced with PCA, PA, CA, or PC extracts (1:10, v/v), and cells were cultured for an additional 48 h. Following treatment, the medium was removed, and the cells were washed twice with PBS. Calcein AM/PI staining working solution (400 μL) was added, followed by 30 min of incubation in the dark. The staining results were observed under CLSM, and live/dead cell counts were quantified using ImageJ.

In parallel, third-passage HDPSCs were seeded into 96-well plates (5×10^3 cells/well) and incubated for 24 h. Cells were then treated with PCA, PA, CA, or PC extracts (1:10, v/v) for 1, 3, and 5 days. At each time point, the medium was replaced with fresh medium containing 10% Cell Counting Kit-8 (CCK-8) reagent and incubated for 2 h. Optical density (OD) was measured at 450 nm, and results were normalized to the control group.

Hemolysis Test

This study was conducted in accordance with ethical approval (QYFYWZLL29632). Healthy human blood samples were collected from the Laboratory Department. One milliliter of blood was diluted with 7 mL PBS, gently mixed, and centrifuged at 1500 rpm for 5 min. The supernatant was removed, and PBS was added to the 8 mL mark along the tube wall. This washing process was repeated four times. On the final wash, no PBS was added after removing the supernatant, resulting in a suspension of red blood cells. Sample preparation included: (A) pure red blood cells and (B) a red blood cell/PBS solution (10%). Test groups were as follows: (i) positive control (total hemolysis), 50 μL A with 950 μL distilled water; (ii) negative control, 500 μL B with 500 μL PBS; (iii) polyelectrolyte complex groups, 500 μL B with 500 μL of each of the PCA, PA, CA, or PC solutions that had been immersed in PBS for 24 h. Each group and control was prepared in triplicate. All samples were incubated at 37 °C for 1.5 h, then centrifuged at 3000 rpm for 15 min. Supernatants were transferred to a 96-well plate, and absorbance was measured at 540 nm. The hemolysis rate (%) was calculated as follows:

$$\text{Hemolysis rate} = (OD_{\text{polyelectrolyte complex}} - OD_{\text{negative}}) / (OD_{\text{positive}} - OD_{\text{negative}}) \times 100\%.$$

Hemolysis rates ≤ 5% meet safety requirements for clinical use.

Statistical Analysis

All data are presented as mean ± standard deviation from at least three independent experiments. Normality was assessed by the Shapiro–Wilk test, and homogeneity of variance was verified with Levene's test. For data meeting normality ($p \geq 0.05$) and homogeneity, one-way ANOVA with Tukey's post hoc test was applied. For non-parametric data, the Kruskal–Wallis test with

Dunn's post hoc correction was used. A two-sided $p < 0.05$ was considered statistically significant ($\alpha = 0.05$). Significance levels are indicated as ns (not significant), $p < 0.05$, or $p < 0.01$. All analyses were performed using IBM SPSS Statistics 27.

Results and Discussion

This study investigated the synergistic mechanism of Pasp and CMC in dentin biomimetic mineralization by constructing their composite system. Experimental results demonstrated that these two polyelectrolytes competitively bind Ca^{2+} ions to form polyelectrolyte complexes (PCA) containing nanoscale ACP. As biomimetic analogs of NCPs, Pasp and CMC effectively stabilized ACP prenucleation clusters and regulated their structure and morphology, enhancing mineralization activity.[14,39] Notably, the incorporation of CMC not only participated in the mineralization process but also inhibited dental plaque biofilm formation through its antibacterial properties. This characteristic is crucial for promoting the penetration of mineralization precursors into dentin.[40] The supplemented Ca^{2+} and PO_4^{3-} ions in the composite system compensated for the deficiency of mineralizing ions in saliva, enhancing overall mineralization capacity.[41,42] In material design, this study systematically compared the performance differences between PCA and three other complexes (PA, CA, and PC) to thoroughly evaluate their application potential in treating DH and caries prevention.

Characterization using HRTEM and SAED revealed the presence of amorphous material in PCA, PA, and CA samples (Figure 1A1–A4), whereas no such component was detected in the PC group (Figure S1A). HRTEM observation showed that the amorphous phase in PCA exhibited the smallest particle size, approximately 2 nm in diameter, which was significantly smaller than those in the PA and CA groups (Figure 1A2). Further SEM coupled with EDS analysis confirmed this amorphous phase as ACP (Figure 1B1–B3, C1–C3, D1–D3), with no ACP characteristic signals observed in the PC group (Figure S1B). The nanoscale ACP clusters in PCA may facilitate better penetration into DTs, suggesting superior tubule-occluding potential. However, the gel-like properties of PCA may partially limit its penetrability, which requires further experimental verification. Of particular note were the Ca/P ratios: PCA (1.67) closely matched the theoretical value for HAP (1.67), whereas PA (1.93) and CA (2.54) showed significant deviations (Figure S2). Given that HAP is the primary inorganic component of dentin, the Ca/P ratio of PCA suggests its potential advantage in promoting biomimetic mineralization. This finding provides critical evidence for PCA's remineralization performance.

XRD analysis confirmed the amorphous nature of PCA, PA, and CA (Figure 1E). Specifically, broad characteristic peaks were observed at $2\theta = 25°$ for PCA, $2\theta = 30°$ for PA, and $2\theta = 24°$ for CA, consistent with the diffraction pattern of ACP. No distinct crystalline diffraction peaks corresponding to HAP or other crystalline calcium phosphate phases were detected, further confirming the amorphous characteristics of these materials.

A higher absolute zeta potential value indicates greater stability. Therefore, PCA demonstrated superior stability compared to PA and CA (Figure 1F), which can be attributed to the synergistic stabilizing effect of Pasp and CMC. The dual-polyelectrolyte system more effectively prevents premature transformation of ACP into crystalline calcium phosphate outside DTs, ensuring sustained release and long-term efficacy of mineralization precursors within DTs. This enhanced stability is crucial for achieving durable biomimetic mineralization.

Under neutral environmental conditions, we measured the concentrations of Ca^{2+} and PO_4^{3-} released by PCA, PA, and CA after 24 h (Figure 1G). The results demonstrated that PA released significantly higher concentrations of Ca^{2+} and PO_4^{3-} compared to the other two groups. Two primary reasons are proposed for this disparity. First, PA contains higher concentrations of Ca^{2+} and PO_4^{3-} than the other two materials. Second, PA exhibits superior fluidity, facilitating easier ion dissociation and diffusion. Although PCA's ion release concentration was lower than PA's, it was markedly higher than CA's. This difference may be attributed to the addition of Pasp in PCA, which enhances rheological properties, and whose carboxyl groups may promote calcium-phosphate ion release through chelation. Ion concentration analysis revealed that the Ca/P ratio remained stable at approximately 1.5, closely matching the characteristic ratio of ACP under neutral pH. This provides strong evidence for the presence of an ACP phase in the materials. Future studies should systematically compare the effects of different material states on ion release kinetics.

FTIR spectroscopy revealed the characteristic functional groups present in PCA, PA, CA, and PC. Specifically, PA exhibited a broad absorption band at 2700–3700 cm^{-1}, attributable to interactions between Ca^{2+} and hydroxyl (-OH) groups in Pasp. Peak shifts in the 1300–1600 cm^{-1} region indicated electrostatic interactions between ACP and both amide (-CO-NH-) and carboxyl (-COOH) groups. Characteristic ACP peaks at 1065 cm^{-1} (ν_3, asymmetric stretching) and

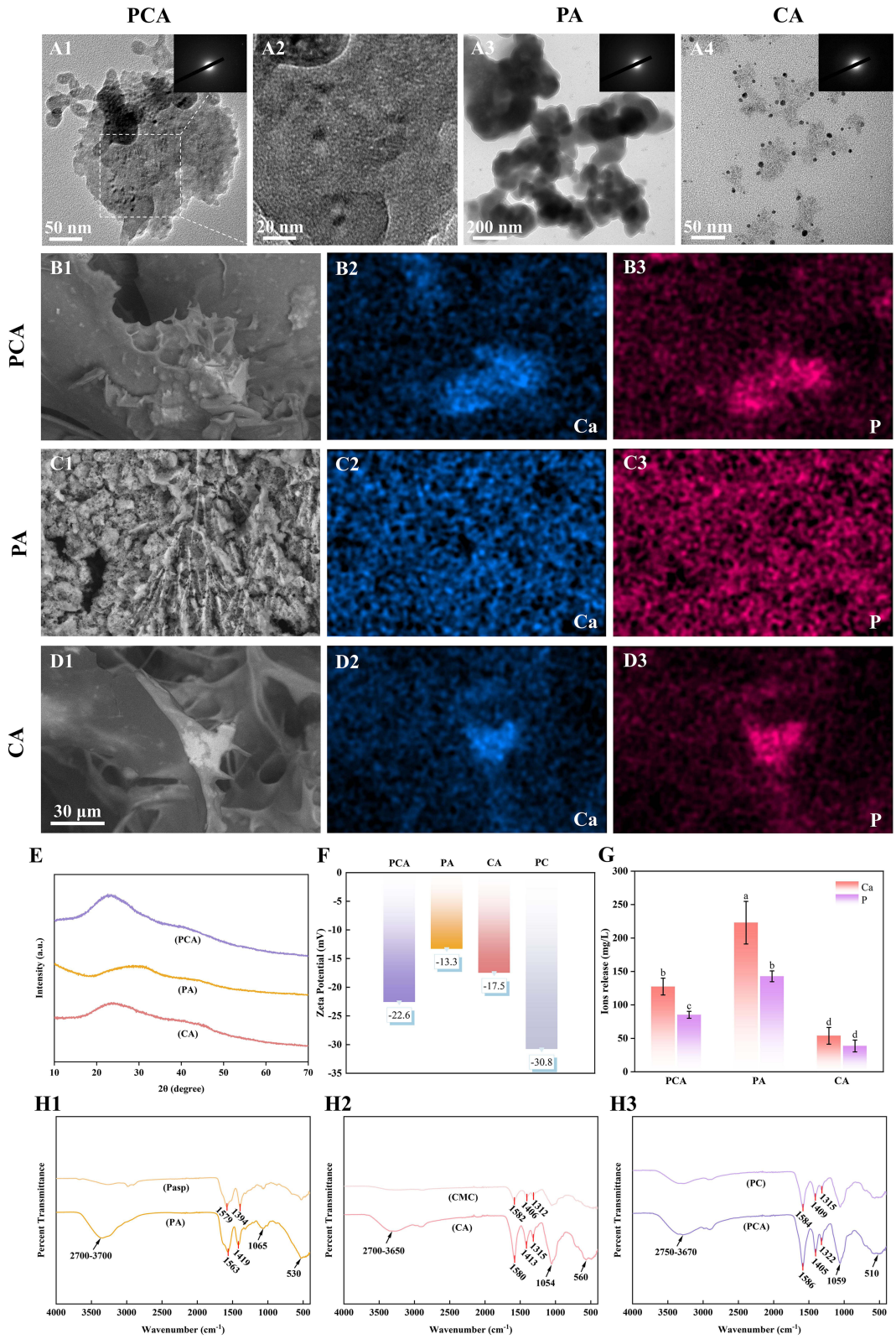

Figure 1 Characterization of PCA, PA, CA, and PC. (**A1**) TEM image of PCA (inset shows SAED pattern). (**A2**) Local magnified TEM image of A1. TEM images of (**A3**) PA and (A4) CA (insets show SAED patterns). (**B1**) SEM image of PCA. EDS mapping images of PCA, (**B2**) calcium, and (**B3**) phosphorus. (**C1**) SEM image of PA. EDS mapping images of PA, (**C2**) calcium, and (**C3**) phosphorus. (**D1**) SEM image of CA. EDS mapping images of CA, (**D2**) calcium, and (**D3**) phosphorus. (**E**) XRD image. (**F**) Zeta potential image. (**G**) Release of Ca and P ions. Different letters denote significant differences ($p < 0.05$). (**H1-3**) FTIR spectra. (See Figure S1 for TEM and SEM images of PC and Figure S3 for FTIR spectra of PC).

530 cm^{-1} (ν_4, bending) confirmed binding between Pasp and ACP. The distinct PO_4^{3-} vibrational modes at these wavenumbers provided direct spectroscopic evidence for successful Pasp-ACP complex formation (Figure 1H1).

For CA samples, the broad absorption peak in the 2700–3650 cm^{-1} range originated from interactions between ACP and both -NH_2 and -OH groups in CMC. In the 1300–1600 cm^{-1} region, peak shifts with enhanced intensity suggested electrostatic interactions between Ca^{2+} and -COOH groups. Characteristic ACP peaks at 1054 cm^{-1} (ν_3) and 560 cm^{-1} (ν_4) further verified CMC-ACP binding. FTIR clearly demonstrated unique PO_4^{3-} vibrational signatures at these positions, conclusively confirming effective CMC-ACP conjugation (Figure 1H2).

PC samples exhibited broad absorption in the 2700–3650 cm^{-1} range, resulting from overlapping -OH/-NH groups of Pasp and electrostatic interactions with CMC's -NH_2 groups. Peak shifts and increased intensity at 1300–1600 cm^{-1} indicated interactions between the -COOH/-CO-NH- groups of Pasp and the -COOH groups of CMC. The peak at 1055 cm^{-1} corresponded to the -C-O- stretching vibrations of secondary hydroxyl (-CH-OH) groups. After Pasp-CMC complexation, characteristic fingerprint peaks at 524 cm^{-1} broadened (Figure S3).

PCA spectra showed broad absorption in the 2700–3700 cm^{-1} region, primarily due to overlapping -OH/-NH groups from Pasp, electrostatic interactions with CMC's -NH_2 groups, and interactions between ACP and the functional groups of both polymers. In the 1300–1600 cm^{-1} range, peak shifts and enhanced intensity confirmed Ca^{2+}-COOH electrostatic binding. The presence of ACP characteristic peaks at 1059 cm^{-1} (ν_3) and 510 cm^{-1} (ν_4) verified ternary complex formation. Distinct PO_4^{3-} vibrational bands at these positions provided definitive evidence for Pasp-CMC-ACP ternary complex formation (Figure 1H3).

As biomimetic analogs of NCPs, polyelectrolytes synergistically guide the ordered deposition of ACP within collagen fibers. Comparative studies using monolayer reconstituted collagen fiber models revealed that PCA, PA, and CA exhibit different mineralization capacities (Figure 2). Combined TEM and SAED analyses demonstrated that after 1 day of

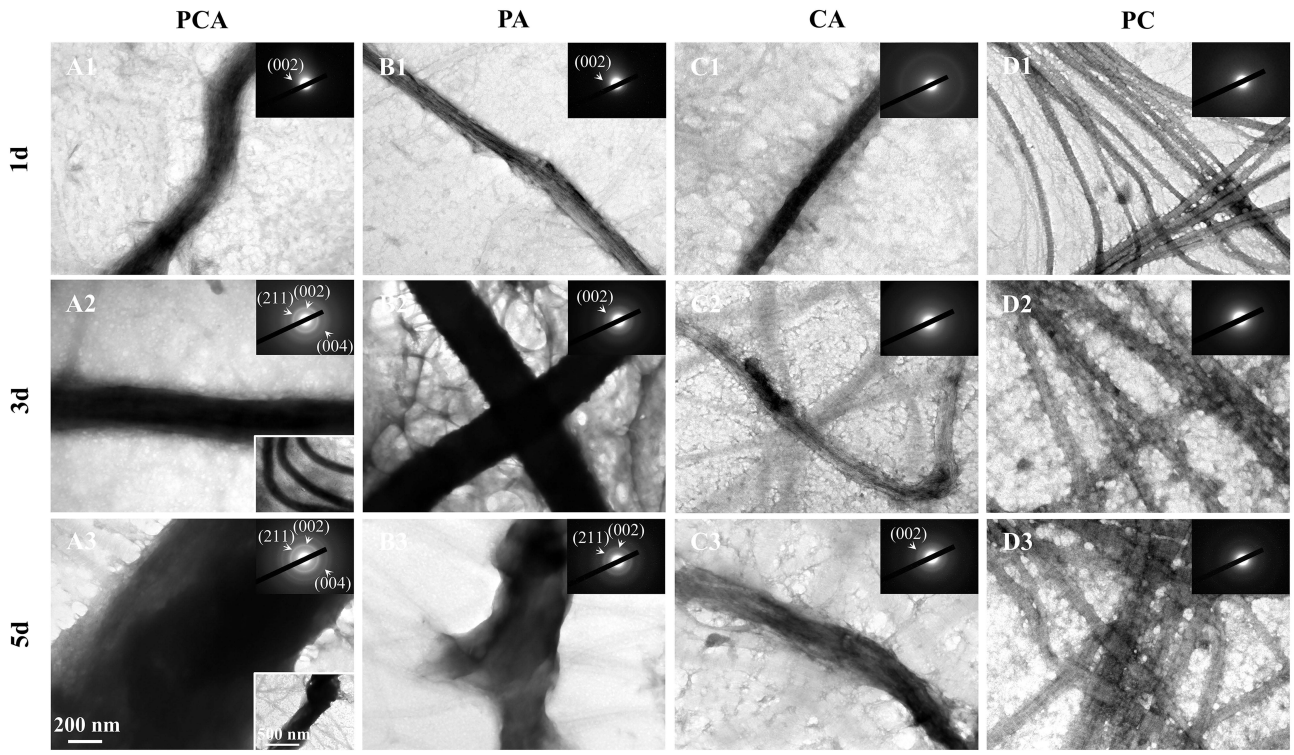

Figure 2 Influence of PCA, PA, CA, and PC on reconstituted collagen. When incubated in PCA for (**A1**) 1, (**A2**) 3, and (**A3**) 5 days, collagen fibers exhibited slight mineralization at 1 day. At 3 days, most collagen fibers were mineralized; at 5 days, the collagen fibers were mineralized entirely. The SAED presented an arcuate diffraction pattern in the (002) and (211) planes. After being incubated in PA for (**B1**) 1, (**B2**) 3, and (**B3**) 5 days, the degree and rate of collagen fiber mineralization were lower than those in PCA. Nevertheless, at 5 days, SAED showed arc-shaped diffraction patterns in the (002) and (211) planes, though these patterns were less distinct than those in PCA. Incubation in CA for (**C1**) 1, (**C2**) 3, and (**C3**) 5 days demonstrated the weakest degree and rate of collagen fiber mineralization. Only some fibers were mineralized at 5 days. During incubation in PC for (**D1**) 1, (**D2**) 3, and (**D3**) 5 days, collagen fibers were not mineralized.

https://doi.org/10.2147/IJN.S530148

incubation, weak arc-shaped diffraction at the (002) crystal plane appeared in the PCA- and PA-treated groups (Figure 2A1 and B1), whereas no significant diffraction signals were detected in the CA group (Figure 2C1). By day 3, the PCA group displayed clear arc-shaped diffraction at both (002) and (211) crystal planes (Figure 2A2), indicating the orderly alignment of HAP crystals along the collagen c-axis, thereby achieving typical intrafibrillar mineralization. In contrast, the PA group showed only (002) plane diffraction (Figure 2B2), whereas the CA group required until day 5 to exhibit weak signals (Figure 2C3). Ultimately, the PCA group achieved complete mineralization (Figure 2A3), outperforming the partial mineralization observed in the PA group (Figure 2B3) and the limited mineralization of the CA group (Figure 2C3). All experimental groups exhibited interfibrillar needle-like crystals, confirming the presence of extrafibrillar mineralization, whereas no mineralization was detected in the PC group throughout (Figure 2D1–D3).

At the molecular level, Pasp facilitates ACP infiltration into fibers via the polymer-induced liquid-precursor (PILP) process.[43–46] The carboxyl groups on its molecular chains may regulate mineralization by interacting with specific collagen sites (eg, -OH, -NH_2),[47] although precise binding sites require further elucidation using techniques such as atomic force microscopy (AFM). CMC influences mineralization through several molecular interactions: its carboxymethyl groups may provide nucleation sites via electrostatic interactions with collagen -NH_2, and molecular forces between -NH_2 and collagen -COOH;[48] concurrently, CMC alters collagen self-assembly kinetics, which may explain its mineralization-promoting mechanism at the material-extracellular matrix interface.[34]

The PCA system demonstrates superior mineralization performance, primarily due to the synergistic effects of Pasp and CMC. Pasp ensures stable ACP infiltration, whereas CMC optimizes the collagen matrix structure and supplies additional nucleation sites. This dual action enables PCA to exceed PA and CA in both mineralization rate and completeness. Notably, the PC group results confirm that Pasp and CMC alone cannot initiate effective mineralization in the absence of ACP, highlighting ACP's essential role in biomimetic mineralization. Although this study provides morphological and structural validation of PCA's mineralization advantages, subsequent mechanical testing, such as nanoindentation, will be necessary to comprehensively evaluate the mechanical enhancement of mineralized collagen, thereby providing a stronger scientific basis for clinical translation.

Through systematic comparison of the mineralization capabilities of four recombinant collagen fibers (PCA, PA, CA, and PC), this study further evaluated their effects on dentin remineralization and DT occlusion through in vitro experiments (Figure 3A). After establishing DH models (see Preparation of DH models), SEM revealed differences in mineralization outcomes among groups after 28 days of treatment.

In the blank group, collagen fibers on the dentin surface remained exposed, with only minimal mineral deposition observed within the tubules and no evidence of mineral penetration into deeper DT regions (Figure 3B1 and B2). The Gluma group exhibited partial surface coverage and a mineral penetration depth of approximately 12 μm, with occasional tubules showing mineral deposits reaching 20–30 μm (Figure 3C1 and C2). The PCA and PA groups showed the most robust surface occlusion effects, achieving complete collagen fiber coverage and intratubular mineralization (Figure 3D1 and E1). The PCA group displayed an average penetration depth of 30 μm (Figure 3D2), whereas the PA group averaged 15 μm, with some DTs exhibiting mineral penetration up to 39 μm (Figure 3E2). The CA group achieved only partial fiber coverage and incomplete tubule occlusion, with a penetration depth of about 15 μm (Figure 3F1 and F2). The PC group, whereas able to cover surface fibers, showed sparse intratubular mineralization with a penetration depth of approximately 5 μm (Figure 3G1 and G2).

In mechanical friction and acid-etching challenge tests, the groups exhibited distinct stability characteristics. The blank group, with initially low mineralization, showed no change in mineral content after treatment (Figure 3B3 and B4). The Gluma group displayed significant mineral loss and fiber re-exposure after acid etching (Figure 3C4). The PCA and PA groups demonstrated exceptional stability, maintaining consistent mineral content after both challenges (Figure 3D3, D4, E3, and E4). The CA group resisted mechanical friction but failed to withstand acid etching (Figure 3F3 and F4), whereas the PC group lost mineral under both challenges (Figure 3G3 and G4). These differences may result from variations in the crystalline structure of the mineralization products.

EDS analysis revealed that the PCA group had a Ca/P ratio of 1.66, closest to the theoretical value of HAP (1.67), indicating successful transformation of ACP into the crystalline form. The PA group (Ca/P ratio: 1.75) and CA group (Ca/P ratio: 1.79)

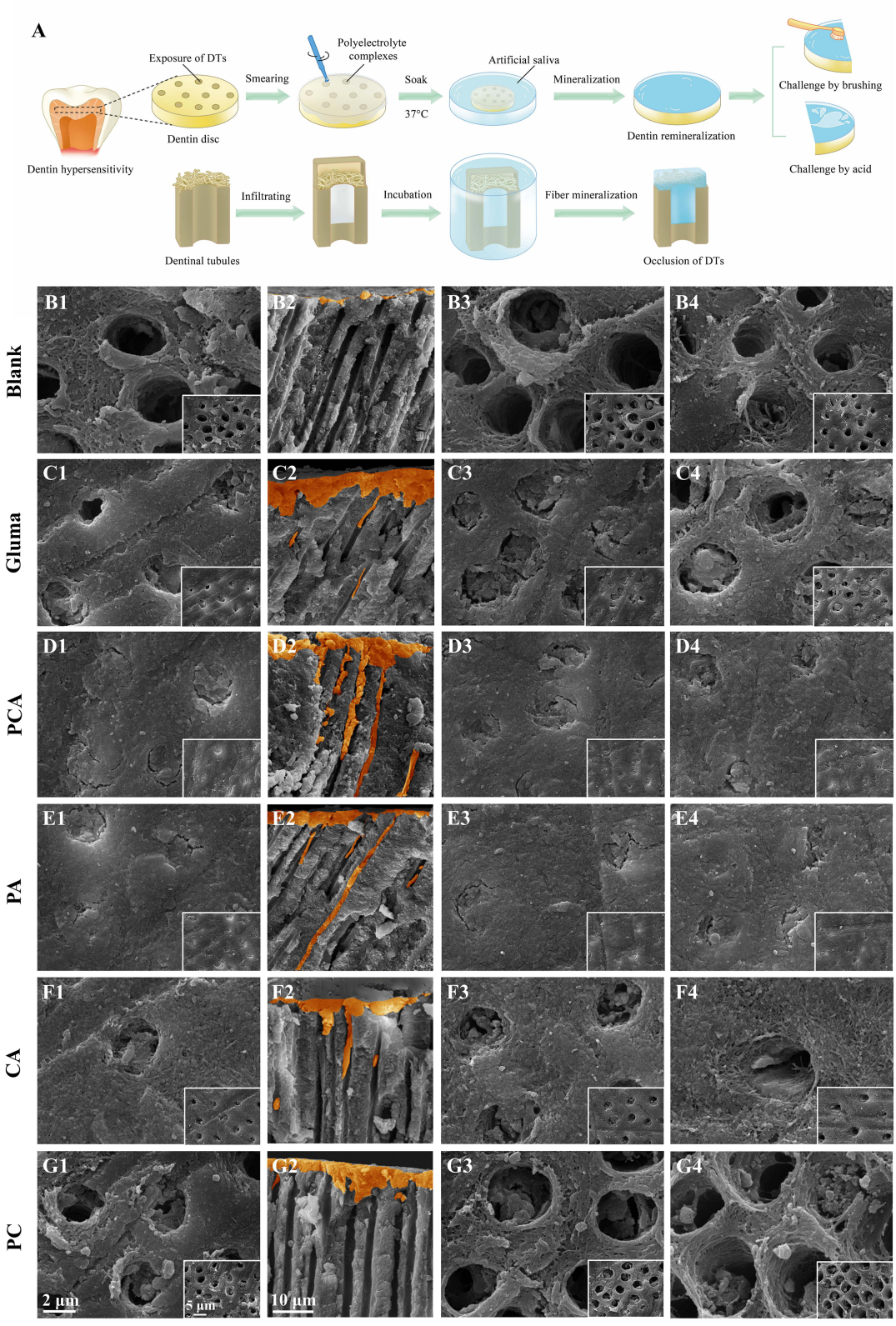

Figure 3 (**A**) Dentin sensitivity models were made and subsequently grouped to treat dentin discs for biomimetic remineralization and the occlusion of DTs. Friction and acid immersion challenges were carried out following 28 days of treatment. SEM images of the (**B1**) dentin surfaces, (**B2**) longitudinal sections, and images (**B3**) post-friction and (**B4**) acid immersion in the blank group after 28 days of treatment. (**C**–**G**) SEM images of the other five groups.

https://doi.org/10.2147/IJN.S530148

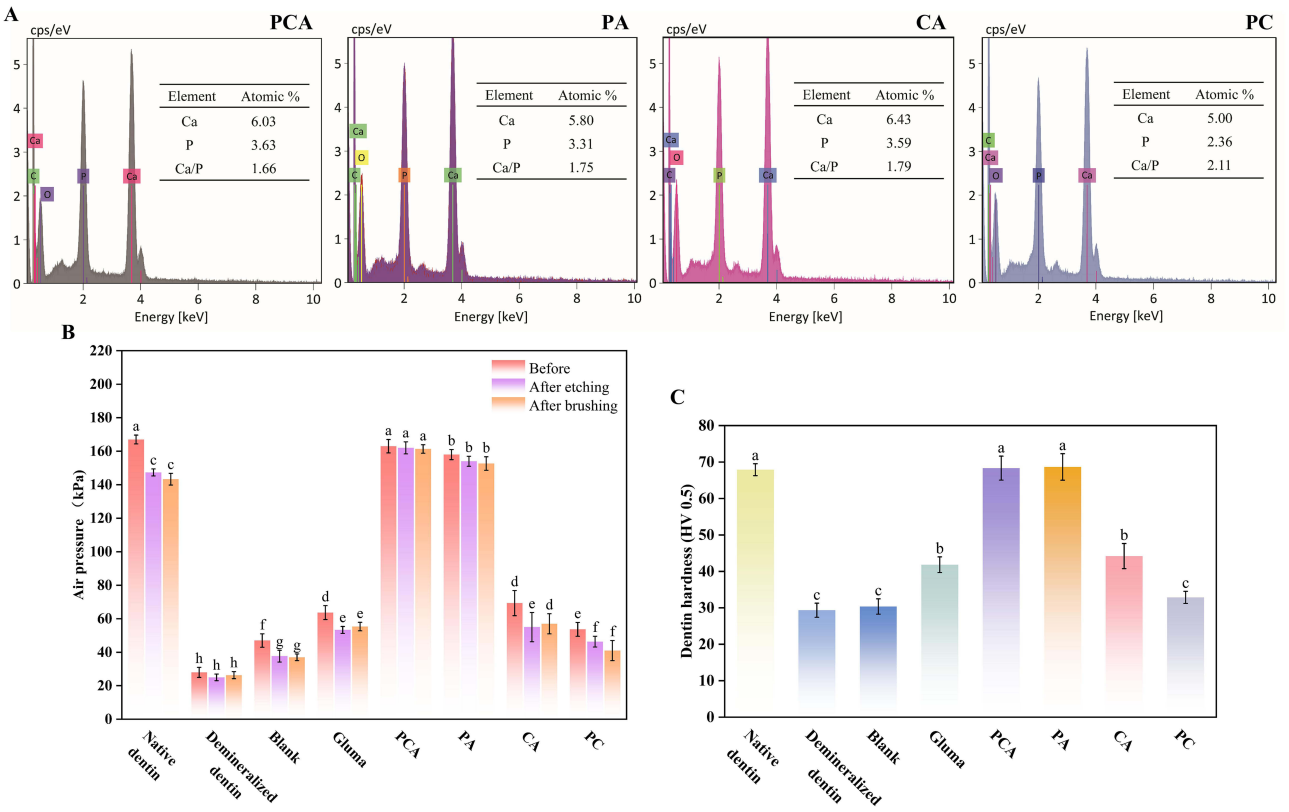

Figure 4 (**A**) Contents of Ca and P in demineralized dentin after incubation with PCA, PA, CA, and PC for 28 days. (**B**) Dentin airtightness data for each group following 28 days of treatment and after friction and acid immersion. Values with different letters indicate significant differences ($p < 0.05$). (**C**) Dentin hardness data for each group after 28 days of treatment. Values with different letters indicate significant differences ($p < 0.05$).

showed slight deviations, suggesting the coexistence of other calcium phosphate phases. In contrast, the abnormally high Ca/P ratio of 2.1 in the PC group confirmed its failure to achieve biomimetic mineralization conversion (Figure 4A).

Dentin primarily consists of organic components such as collagen and NCPs.[49] At the molecular level, Pasp, containing aspartic acid residues as an NCP analog, promotes remineralization through a dual mechanism: (1) its acidic domain stabilizes ACP and accelerates its conversion to HAP, reducing the remineralization cycle from 7 days to 2 days;[50] and (2) it specifically recognizes collagen active sites to form mineralization nucleation centers.[47] Capillary effects further facilitate deep penetration into DTs for physical occlusion. CMC also exhibits NCP-mimicking functionality, but its poor flow properties limit penetration depth, explaining why Pasp-containing PA outperformed CMC-containing CA in occlusion depth. Notably, the superior resistance to friction and acid etching observed in the PCA and PA groups confirms a correlation between mineralization quality and clinical durability.

This study selected Gluma as a positive control to reflect the occlusion efficacy of clinically effective materials. However, its protein precipitation mechanism differs from the biomimetic mineralization approach used here. Future studies will incorporate additional control groups for more comprehensive comparisons, including positive controls for remineralization mechanisms. Optimizing the fluidity of CMC may also enable deeper and more durable tubule occlusion.

The study optimized a dentin sealing test device, employing an air pressure measurement method to evaluate dentin sealing ability and DT permeability, whereas comparing the sealing efficacy of different treatment groups. After 28 days of treatment, followed by acid immersion and abrasion, dentin sealing ability was assessed. The PCA group showed no significant difference in dentin sealing ability compared to normal dentin ($p \geq 0.05$), and its performance remained stable after acid immersion and abrasion, indicating that PCA effectively restored dentin sealing (Figure 4B). In contrast, the PA group exhibited significantly lower sealing ability than normal dentin ($p < 0.05$), but no further decline was observed after acid immersion and abrasion. The blank control, Gluma, CA, and PC groups demonstrated improved sealing compared to the demineralized group, yet all remained significantly lower than normal dentin ($p < 0.05$). Furthermore,

their performance declined further after acid immersion and abrasion, suggesting limited efficacy in restoring dentin sealing. These test results aligned with the findings for remineralization and tubule occlusion, confirming that PCA effectively restored the structural integrity of demineralized dentin.

For mechanical properties, Vickers hardness testing showed that dentin hardness in the PCA and PA groups was significantly higher than that of the demineralized group ($p < 0.05$) and did not differ significantly from normal dentin ($p \geq 0.05$), indicating effective restoration of dentin mechanical performance (Figure 4C). The Gluma and CA groups exhibited higher hardness than the demineralized group, but values remained significantly lower than those of normal dentin ($p < 0.05$), with no significant difference between Gluma and CA ($p \geq 0.05$), suggesting limited restorative effects. The blank control and PC groups showed no significant difference in hardness compared to the demineralized group ($p \geq 0.05$) and were significantly lower than all other treatment groups ($p < 0.05$), indicating a lack of effective restoration of dentin mechanical properties.

These comprehensive results demonstrate that PCA and PA not only provide durable DT occlusion and significantly enhance sealing but also effectively improve dentin mechanical properties, making the tissue more resistant to mechanical and chemical stimuli in the oral environment. This dual mechanism supports both the treatment and prevention of DH recurrence. In contrast, CA showed efficacy comparable to that of Gluma, a commonly used clinical desensitizer, whereas PC lacking ACP produced almost no noticeable therapeutic effect.

Dental plaque biofilm formation is closely associated with the initiation and progression of dental caries, with *S. mutans* recognized as a major pathogenic bacterium due to its strong acidogenicity, acid tolerance, and capacity for extracellular polysaccharide synthesis.[51] In this study, *S. mutans* was anaerobically cultured for 36 h, followed by treatment with deionized water (control), PCA, CA, or PC for an additional 24 h to systematically evaluate effects on plaque biofilm. CLSM revealed that the dentin surface in the control group was fully covered by viable bacteria (green fluorescence), whereas the PCA, CA, and PC groups exhibited significantly reduced viable bacterial coverage ($p < 0.05$) and increased proportions of dead bacteria (red fluorescence) ($p < 0.05$) (Figure 5A and B). No significant difference in total biofilm biomass was observed among the PCA, CA, and PC groups ($p \geq 0.05$) (Figure 5C). SEM confirmed reduced *S. mutans* adhesion on dentin surfaces in the treatment groups (Figure 5D). Colony-forming unit (CFU) counts showed that, after 12 and 24 h of incubation, bacterial counts in the PCA, CA, and PC groups were significantly lower than in the control group ($p < 0.05$) (Figure 5E and F). These findings indicate that PCA, CA, and PC effectively inhibit *S. mutans* biofilm formation and demonstrate bactericidal activity.

The antibacterial mechanism of CMC likely operates through multiple pathways.[52,53] Positively charged CMC molecules disrupt bacterial membrane integrity via electrostatic interactions with phospholipids, inhibit key metabolic enzymes (eg, respiratory and synthetase enzymes), and interfere with genetic replication by binding to nucleic acids. CMC may also activate bacterial autolysin systems or apoptotic pathways. Notably, although PC was expected to demonstrate superior antibacterial efficacy due to its higher CMC content, the experimental data showed no significant difference among the three groups. This observation may be explained by the synergistic effects of Ca^{2+} and PO_4^{3-} released by PCA and CA: Ca^{2+} destabilizes bacterial membranes by binding to anionic components, whereas PO_4^{3-} modulates the microenvironmental pH to suppress bacterial growth. PCA and CA may also provide sustained ion release at the bacterial surface, enhancing antibacterial persistence.

Regarding experimental design, a blank control was used to minimize interference from the culture medium and environmental factors. Subsequent investigations will prioritize comparisons with existing commercial products to assess clinical applicability. Additionally, future studies will include synergistic antibacterial agents and develop multispecies biofilm models to better mimic the oral microecological environment, thereby optimizing antibacterial efficacy.

To evaluate the cytotoxicity of PCA, PA, CA, and PC, HDPSCs were successfully isolated and cultured from extracted teeth. The isolated cells displayed typical spindle-shaped morphology (Figure S4) and, as confirmed by flow cytometry, met the criteria of HDPSCs: high expression of mesenchymal stem cell markers (CD73, CD90, and CD95, all > 95% positivity) and low expression of hematopoietic lineage markers (CD34 and CD45, both < 2% positivity) (Figure S5).

Live/dead fluorescence staining showed good cell viability across the PCA, PA, CA, and PC groups, with no significant differences in the proportions of live or dead cells compared to the control ($p \geq 0.05$) (Figure 6A and B). The CCK-8 assay further confirmed that HDPSC viability in all groups did not differ significantly from the control ($p \geq 0.05$) (Figure 6C), indicating no apparent inhibitory effect on cell growth. Additionally, hemolysis testing revealed that

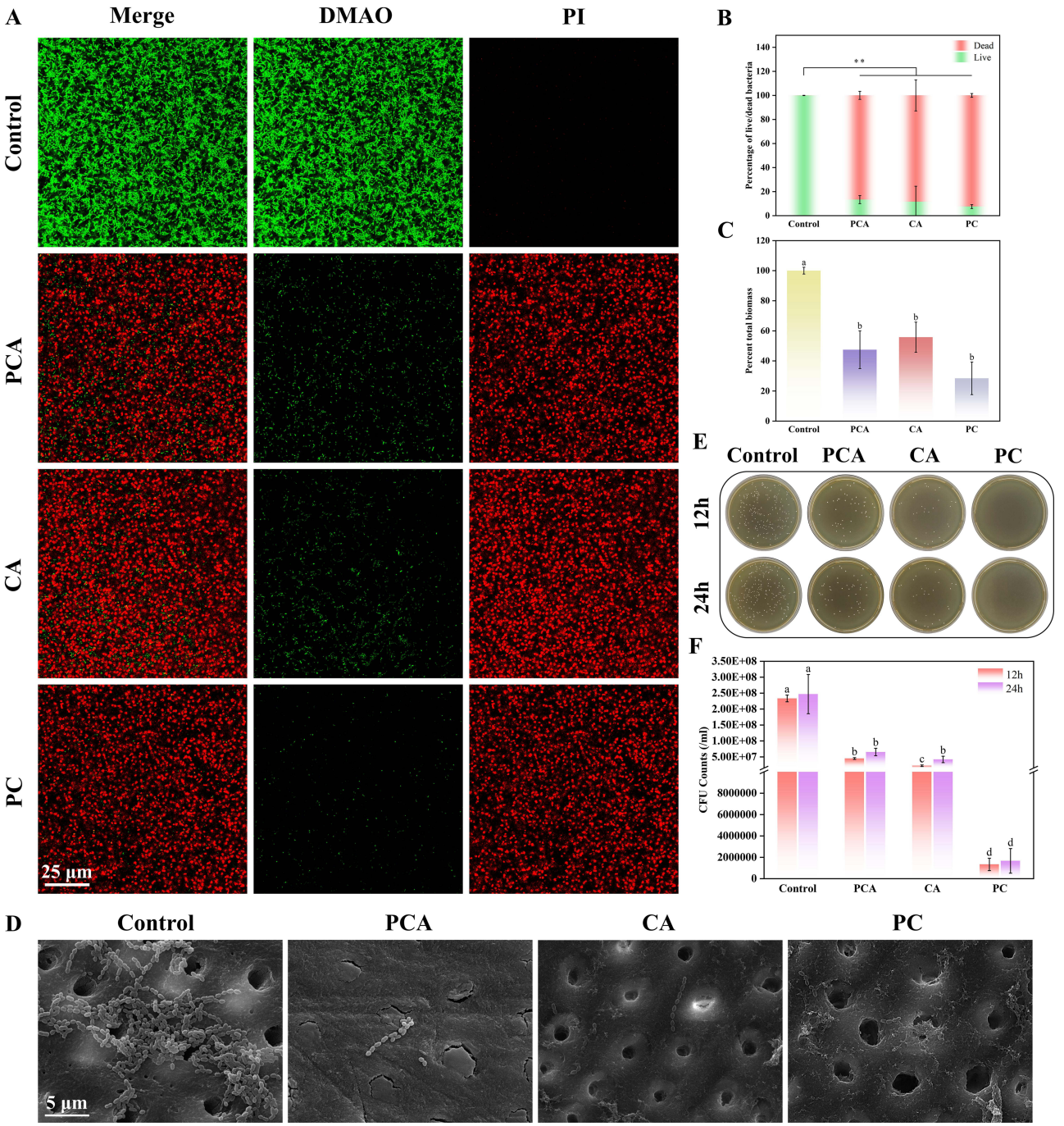

Figure 5 (**A**) CLSM images of live/dead bacterial staining for the Control, PCA, CA, and PC groups. Live bacteria were stained green with DMAO, while dead bacteria were stained red with PI. (**B**) The percentage of live/dead bacteria in each group (** $p < 0.01$). (**C**) The percentage of live bacteria relative to the total number of bacteria in each group. Values with different letters indicate significant differences ($p < 0.05$). (**D**) SEM images of bacteria adhering to the surface of dentin discs in each group. (**E**) Representative photographs of each group of *S. mutans* colonies grown on BHI agar plates. (**F**) CFU counts. Values with different letters indicate significant differences ($p < 0.05$).

hemolysis rates for all groups were below 5% (Figure 6D and E), meeting established safety standards for biomaterials. These results collectively demonstrate that PCA, PA, CA, and PC exhibit good cytocompatibility and hemocompatibility.

CMC, as a polyelectrolyte, serves multiple roles in regulating HDPSC behavior. Studies show that CMC, when combined with nano-hydroxyapatite (nHAP) to form a composite scaffold, not only promotes HDPSC adhesion and proliferation but also significantly upregulates the expression of odontogenic markers such as DSPP, dentin matrix protein-1 (DMP-1), alkaline phosphatase (ALP), and vascular endothelial growth factor (VEGF), thereby enhancing

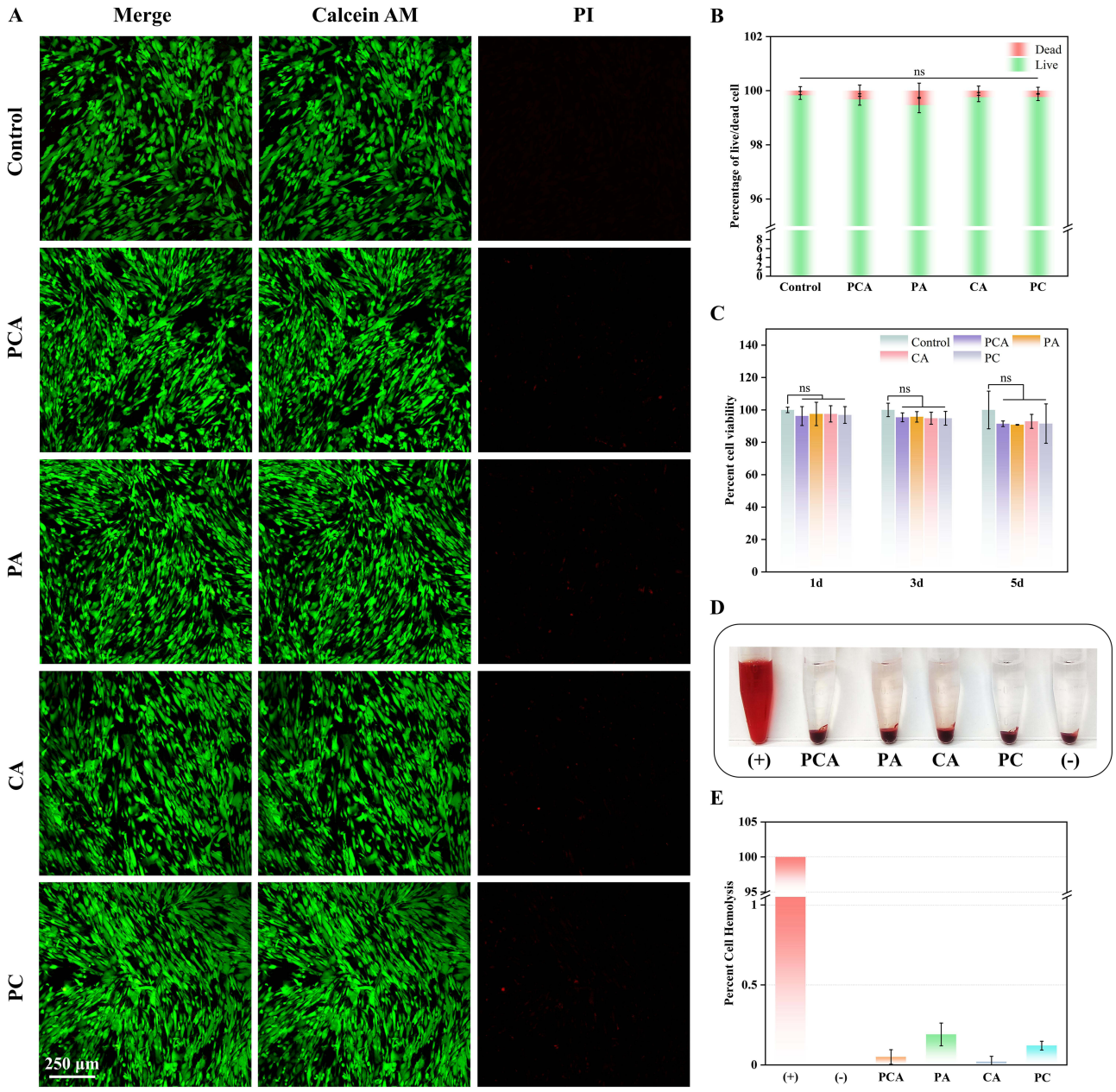

Figure 6 (**A**) CLSM images of live/dead cell staining for the Control, PCA, PA, CA, and PC groups. Live cells were stained green with Calcein AM, while dead cells were stained red with PI. (**B**) The percentage of live/dead cells in each group (ns = not significant). (**C**) CCK-8 results for HDPSCs in each group over 1, 3, and 5 days (ns = not significant). (**D**) Representative photographs of the hemolysis experiments in each group. (**E**) The percentage of the hemolysis rate in each group.

mineralization and tissue regeneration.[54,55] This may occur via a polyelectrolyte-induced "cell aggregation phenomenon", in which cells form high-density aggregates through electrostatic interactions within the CMC microenvironment, enhancing intercellular communication and differentiation synergy. Future research should investigate the association between polyelectrolyte charge density and the spatiotemporal dynamics of cell aggregation to optimize biomimetic mineralization strategies.

PCA demonstrates unique advantages in treating DH and caries prevention. Its biomimetic remineralization mechanism forms mineral structures closely resembling natural HAP, effectively occluding DTs and repairing demineralized tooth structures, thereby providing durable therapeutic effects. Experimental data confirm that PCA significantly promotes dentin remineralization and exhibits antibacterial properties that inhibit cariogenic bacterial growth, achieving both DH relief and caries prevention. Compared with conventional desensitizing agents, PCA shows long-term efficacy.

https://doi.org/10.2147/IJN.S530148

And PCA has superior biocompatibility. To further validate clinical applicability, future studies will employ experimental models that better simulate actual oral conditions, including extended mechanical-chemical challenge cycles, multi-species biofilm systems, and dynamic simulation for functional assessment, as well as animal experiments under near-physiological conditions. These improvements will support more accurate prediction of PCA's performance in complex oral environments, providing stronger evidence for clinical application.

Conclusion

PCA emerges as a promising multifunctional agent for dental applications. Its ability to effectively promote dentin remineralization and occlude DTs positions it as a viable solution for the treatment and prevention of DH. Additionally, PCA's inherent antimicrobial properties contribute to caries prevention by inhibiting bacterial growth. These dual benefits —biomimetic mineralization and antibacterial activity—highlight PCA's potential as a superior alternative to conventional desensitizing agents. However, further in vivo studies and long-term clinical evaluations are required to validate its safety, stability, and practical utility. Future research could also explore synergistic combinations with other bioactive materials to enhance therapeutic efficacy.

Ethics Approval and Informed Consent

This study was conducted in accordance with the principles of the Declaration of Helsinki. The Medical Ethics Committee of the Affiliated Hospital of Qingdao University approved the study protocol (QYFYWZLL29632). Informed consent has been obtained from the donors of the extracted teeth and blood samples.

Acknowledgments

The study was funded by grants from the Youth Innovation Team Program of Universities in Shandong Province (2022KJ297).

Disclosure

The authors declare that this study is not associated with any conflicts of interest.

References

1. Bergamini MR, Bernardi MM, Sufredini IB, et al. Dentin hypersensitivity induces anxiety and increases corticosterone serum levels in rats. *Life Sci*. 2014;98(2):96–102. doi:10.1016/j.lfs.2014.01.004
2. Tolentino AB, Zeola LF, Fernandes MRU, Pannuti CM, Soares PV, Aranha ACC. Photobiomodulation therapy and 3% potassium nitrate gel as treatment of cervical dentin hypersensitivity: a randomized clinical trial. *Clin Oral Investig*. 2022;26(12):6985–6993. doi:10.1007/s00784-022-04652-1
3. Marto CM, Baptista Paula A, Nunes T, et al. Evaluation of the efficacy of dentin hypersensitivity treatments-A systematic review and follow-up analysis. *J Oral Rehabil*. 2019;46(10):952–990. doi:10.1111/joor.12842
4. West NX, Seong J, Davies M. Management of dentine hypersensitivity: efficacy of professionally and self-administered agents. *J Clin Periodontol*. 2015;42(16):S256–302. doi:10.1111/jcpe.12336
5. Shao C, Jin B, Mu Z, et al. Repair of tooth enamel by a biomimetic mineralization frontier ensuring epitaxial growth. *Sci Adv*. 2019;5(8):eaaw9569. doi:10.1126/sciadv.aaw9569
6. Wang Q, Wang G, Li X, Li D, Zhang C, Ding J. Photothermal Effect and Biomineralization of Black Phosphorus Nanosheet-Composited Hydrogel Boosts Synergistic Treatment of Dentin Hypersensitivity. *Adv Sci*. 2025;12(9):e2412561. doi:10.1002/advs.202412561
7. Pang Y, Fu C, Zhang D, et al. Biomimetic Remineralization of Dental Hard Tissues via Amyloid-Like Protein Matrix Composite with Amorphous Calcium Phosphate. *Adv Funct Mater*. 2024;34(39):2403233. doi:10.1002/adfm.202403233
8. Muşat V, Anghel EM, Zaharia A, et al. A Chitosan-Agarose Polysaccharide-Based Hydrogel for Biomimetic Remineralization of Dental Enamel. *Biomolecules*. 2021;11(8):1137. doi:10.3390/biom11081137
9. Li B, Xu J, Ai R, et al. Safe and Durable Treatment of Dentin Hypersensitivity via Nourishing and Remineralizing Dentin Based on β-Chitooligosaccharide Graft Derivative. *Small*. 2023;19(41):e2300359. doi:10.1002/smll.202300359
10. Tay FR, Pashley DH. Guided tissue remineralisation of partially demineralised human dentine. *Biomaterials*. 2008;29(8):1127–1137. doi:10.1016/j.biomaterials.2007.11.001
11. Aruna Rani SV, Rajkumar K, Saravana Karthikeyan B, Mahalaxmi S, Rajkumar G, Dhivya V. Micro-Raman spectroscopy analysis of dentin remineralization using eggshell derived nanohydroxyapatite combined with phytosphingosine. *J Mech Behav Biomed Mater*. 2023;141:105748. doi:10.1016/j.jmbbm.2023.105748
12. Saravana Karthikeyan B, Mahalaxmi S. Biomimetic dentin remineralization using eggshell derived nanohydroxyapatite with and without carboxymethyl chitosan - An in vitro study. *Int J Biol Macromol*. 2024;270(Pt 1):132359. doi:10.1016/j.ijbiomac.2024.132359
13. Yu L, Wei M. Biomineralization of Collagen-Based Materials for Hard Tissue Repair. *Int J Mol Sci*. 2021;22(2):944. doi:10.3390/ijms22020944

14. Zhang Q, Guo J, Huang Z, Mai S. Promotion Effect of Carboxymethyl Chitosan on Dental Caries via Intrafibrillar Mineralization of Collagen and Dentin Remineralization. *Materials (Basel)*. 2022;15(14):4835. doi:10.3390/ma15144835
15. Liu Y, Li N, Qi YP, et al. Intrafibrillar collagen mineralization produced by biomimetic hierarchical nanoapatite assembly. *Adv Mater*. 2011;23 (8):975–980. doi:10.1002/adma.201003882
16. Kinney JH, Habelitz S, Marshall SJ, Marshall GW. The importance of intrafibrillar mineralization of collagen on the mechanical properties of dentin. *J Dent Res*. 2003;82(12):957–961. doi:10.1177/154405910308201204
17. Prasad M, Butler WT, Qin C. Dentin sialophosphoprotein in biomineralization. *Connect Tissue Res*. 2010;51(5):404–417. doi:10.3109/03008200903329789
18. Liu MM, Li WT, Xia XM, Wang F, MacDougall M, Chen S. Dentine sialophosphoprotein signal in dentineogenesis and dentine regeneration. *Eur Cell Mater*. 2021;42:43–62. doi:10.22203/eCM.v042a04
19. Wang Y, Azaïs T, Robin M, et al. The predominant role of collagen in the nucleation, growth, structure and orientation of bone apatite. *Nat Mater*. 2012;11(8):724–733. doi:10.1038/nmat3362
20. Yu L, Martin IJ, Kasi RM, Wei M. Enhanced Intrafibrillar Mineralization of Collagen Fibrils Induced by Brushlike Polymers. *ACS Appl Mater Interfaces*. 2018;10(34):28440–28449. doi:10.1021/acsami.8b10234
21. Wang Y, Zhang Y, Shen Z, et al. STMP and PVPA as Templating Analogs of Noncollagenous Proteins Induce Intrafibrillar Mineralization of Type I Collagen via PCCP Process. *Adv Healthc Mater*. 2024;13(20):e2400102. doi:10.1002/adhm.202400102
22. Wu H, Shao C, Shi J, et al. Hyaluronic acid-mediated collagen intrafibrillar mineralization and enhancement of dentin remineralization. *Carbohydr Polym*. 2023;319:121174. doi:10.1016/j.carbpol.2023.121174
23. Xie H, Sun J, Xie F, He S. Intrafibrillar mineralization of type I collagen by micelle-loaded amorphous calcium phosphate nanoparticles. *RSC Adv*. 2023;13(17):11733–11741. doi:10.1039/d3ra01321a
24. Wu L, Wang Q, Li Y, et al. A Dopamine Acrylamide Molecule for Promoting Collagen Biomimetic Mineralization and Regulating Crystal Growth Direction. *ACS Appl Mater Interfaces*. 2021;13(33):39142–39156. doi:10.1021/acsami.1c12412
25. Cantaert B, Beniash E, Meldrum FC. The Role of Poly(Aspartic Acid) in the Precipitation of Calcium Phosphate in Confinement. *J Mater Chem B*. 2013;1(48):6586. doi:10.1039/c3tb21296c
26. Pina S, Oliveira JM, Reis RL. Natural-based nanocomposites for bone tissue engineering and regenerative medicine: a review. *Adv Mater*. 2015;27 (7):1143–1169. doi:10.1002/adma.201403354
27. Lotsari A, Rajasekharan AK, Halvarsson M, Andersson M. Transformation of amorphous calcium phosphate to bone-like apatite. *Nat Commun*. 2018;9(1):4170. doi:10.1038/s41467-018-06570-x
28. Yao S, Lin X, Xu Y, et al. Osteoporotic Bone Recovery by a Highly Bone-Inductive Calcium Phosphate Polymer-Induced Liquid-Precursor. *Adv Sci*. 2019;6(19):1900683. doi:10.1002/advs.201900683
29. Takahashi N, Nyvad B. Ecological Hypothesis of Dentin and Root Caries. *Caries Res*. 2016;50(4):422–431. doi:10.1159/000447309
30. Love RM, Tanner ACR. Microbiology of Dental Caries and Dentinal Tubule Infection. *Endodontic Microbiology*. 2017;2017:25–49.
31. Ricucci D, Siqueira Jr JF, Li Y, Tay FR. Vital pulp therapy: histopathology and histobacteriology-based guidelines to treat teeth with deep caries and pulp exposure. *J Dent*. 2019;86:41–52. doi:10.1016/j.jdent.2019.05.022
32. Liu G, Wu C, Abrams WR, Li Y. Structural and Functional Characteristics of the Microbiome in Deep-Dentin Caries. *J Dent Res*. 2020;99 (6):713–720. doi:10.1177/0022034520913248
33. Mi C, Jing Z, Zhu W. A novEl Universal adhesive for improved dentin remineralization with antibiofilm potential against Streptococcus mutans and other cariogenic-pathogens. *Int J Adhes Adhes*. 2022;118:103189. doi:10.1016/j.ijadhadh.2022.103189
34. Liu H, Lin M, Liu X, et al. Doping bioactive elements into a collagen scaffold based on synchronous self-assembly/mineralization for bone tissue engineering. *Bioact Mater*. 2020;5(4):844–858. doi:10.1016/j.bioactmat.2020.06.005
35. TM MW, Lau WM, Khutoryanskiy VV. Chitosan and Its Derivatives for Application in Mucoadhesive Drug Delivery Systems. *Polymers*. 2018;10 (3):267. doi:10.3390/polym10030267
36. Chen Z, Cao S, Wang H, et al. Biomimetic remineralization of demineralized dentine using scaffold of CMC/ACP nanocomplexes in an in vitro tooth model of deep caries. *PLoS One*. 2015;10(1):e0116553. doi:10.1371/journal.pone.0116553
37. Shariatinia Z. Carboxymethyl chitosan: properties and biomedical applications. *Int J Biol Macromol*. 2018;120(Pt B):1406–1419. doi:10.1016/j.ijbiomac.2018.09.131
38. Bu N, Zhou N, Cao G, et al. Konjac glucomannan/carboxymethyl chitosan film embedding gliadin/casein nanoparticles for grape preservation. *Int J Biol Macromol*. 2023;249:126131. doi:10.1016/j.ijbiomac.2023.126131
39. Li Y, Dong J, Zhan W, et al. Constructing the Enamel-Like Dentin Adhesion Interface to Achieve Durable Resin-Dentin Adhesion. *ACS Nano*. 2024;18(43):30031–30052. doi:10.1021/acsnano.4c11224
40. He J, Bao Y, Li J, Qiu Z, Liu Y, Zhang X. Nanocomplexes of carboxymethyl chitosan/amorphous calcium phosphate reduce oral bacteria adherence and biofilm formation on human enamel surface. *J Dent*. 2019;80:15–22. doi:10.1016/j.jdent.2018.11.003
41. Combes C, Rey C. Amorphous calcium phosphates: synthesis, properties and uses in biomaterials. *Acta Biomater*. 2010;6(9):3362–3378. doi:10.1016/j.actbio.2010.02.017
42. Gelli R, Ridi F, Baglioni P. The importance of being amorphous: calcium and magnesium phosphates in the human body. *Adv Colloid Interface Sci*. 2019;269:219–235. doi:10.1016/j.cis.2019.04.011
43. Quan BD, Sone ED. The effect of polyaspartate chain length on mediating biomimetic remineralization of collagenous tissues. *J R Soc Interface*. 2018;15(147):20180269. doi:10.1098/rsif.2018.0269
44. Chen Z, Duan Y, Shan S, et al. Deep and compact dentinal tubule occlusion via biomimetic mineralization and mineral overgrowth. *Nanoscale*. 2022;14(3):642–652. doi:10.1039/d1nr05479a
45. Thula TT, Svedlund F, Rodriguez DE, Podschun J, Pendi L, Gower LB. Mimicking the Nanostructure of Bone: comparison of Polymeric Process-Directing Agents. *Polymers*. 2011;3(1):10–35. doi:10.3390/polym3010010
46. Burwell AK, Thula-Mata T, Gower LB, et al. Functional remineralization of dentin lesions using polymer-induced liquid-precursor process. *PLoS One*. 2012;7(6):e38852. doi:10.1371/journal.pone.0038852
47. Quan BD, Wojtas M, Sone ED. Polyaminoacids in Biomimetic Collagen Mineralization: roles of Isomerization and Disorder in Polyaspartic and Polyglutamic Acids. *Biomacromolecules*. 2021;22(7):2996–3004. doi:10.1021/acs.biomac.1c00402

48. Li Z, Zeng Y, Ren Q, et al. Mineralization promotion and protection effect of carboxymethyl chitosan biomodification in biomimetic mineralization. *Int J Biol Macromol*. 2023;234:123720. doi:10.1016/j.ijbiomac.2023.123720
49. Tao S, Yang J, Su Z, et al. A Dentin Biomimetic Remineralization Material with an Ability to Stabilize Collagen. *Small*. 2022;18(38):e2203644. doi:10.1002/smll.202203644
50. Zhao L, Sun J, Zhang C, et al. Effect of aspartic acid on the crystallization kinetics of ACP and dentin remineralization. *J Mech Behav Biomed Mater*. 2021;115:104226. doi:10.1016/j.jmbbm.2020.104226
51. Gao Z, Chen X, Wang C, et al. New strategies and mechanisms for targeting Streptococcus mutans biofilm formation to prevent dental caries: a review. *Microbiol Res*. 2023;278:127526. doi:10.1016/j.micres.2023.127526
52. Verlee A, Mincke S, Stevens CV. Recent developments in antibacterial and antifungal chitosan and its derivatives. *Carbohydr Polym*. 2017;164:268–283. doi:10.1016/j.carbpol.2017.02.001
53. Li J, Zhuang S. Antibacterial activity of chitosan and its derivatives and their interaction mechanism with bacteria: current state and perspectives. *Eur Polym J*. 2020;138:109984. doi:10.1016/j.eurpolymj.2020.109984
54. Gurucharan I, Saravana Karthikeyan B, Mahalaxmi S, et al. Characterization of nano-hydroxyapatite incorporated carboxymethyl chitosan composite on human dental pulp stem cells. *Int Endod J*. 2023;56(4):486–501. doi:10.1111/iej.13885
55. Saravana Karthikeyan B, Madhubala MM, Rajkumar G, et al. Physico-chemical and biological characterization of synthetic and eggshell derived nanohydroxyapatite/carboxymethyl chitosan composites for pulp-dentin tissue engineering. *Int J Biol Macromol*. 2024;271(Pt 1):132620. doi:10.1016/j.ijbiomac.2024.132620